Integrated design of negative stiffness honeycomb structures considering performance and operational degradation

Hyung-Do Kim[1], Taemin Noh[2], Young-Jin Kang[3], Nam-Ho Kim[4], and Yoojeong Noh[5*]

[1,2,5] *School of Mechanical Engineering Pusan National University, Busan, 46241, South Korea*

kimhd97@pusan.ac.kr
nohtm71@naver.com
yoonoh@pusan.ac.kr (Corresponding author)

[4] *Department of Mechanical and Aerospace Engineering, University of Florida, Gainesville, 32611, USA*

nkim@ufl.edu

[3] *Research Institute of Mechanical Technology, Pusan National University, Busan, 46241, South Korea*

zmanx@pusan.ac.kr

ABSTRACT

This study introduces an integrated framework for conceptualizing the design of negative stiffness honeycomb (NSH) structures, specifically considering the durability and performance of their unit cells. Unlike conventional energy-absorbing structures that rely on plastic deformation, NSH offers a promising alternative for reusable energy absorption (EA) and high initial stiffness, making it suitable for a wide range of engineering applications. The research considers the variability in characteristics of NSH based on the shape of the configured negative stiffness beam (NSB), selecting a single curved-beam unit cell as the focal point. Extensive testing, including quasi-static and cyclic compression tests, is conducted on NSH unit cell fabricated using polylactic acid/polyhydroxy alkenoate (PLA/PHA) filament, to analyze performance under stress and to assess degradation over time. Central to the study is the use of multi-objective optimization (MOO) to explore the trade-off between performance and operational durability, thereby emphasizing the significance of degradation in the design process. The results demonstrate the potential for NSH structures, particularly in terms of their reusability and efficiency, highlighting the viability of incorporating durability considerations in the early stages of design, especially for structures intended for additive manufacturing processes.

1. INTRODUCTION

NSH structures exhibit unique characteristics when compared to traditional hexagonal honeycombs. While hexagonal honeycombs effectively absorb energy through plastic deformation, they fall short in terms of reusability

post-deformation. (Correa et al., 2015) NSH structures, composed of NSBs, stand out for their recoverable energy absorption, as highlighted by (Klatt et al., 2013; Correa et al., 2015), their high initial stiffness (Correa et al., 2015), and their capabilities in impact isolation (Shan et al., 2015; Debeau et al., 2018), creating opportunities for their use in many engineering fields.

Many studies have been conducted on the characteristics of such NSBs. Qiu et al. (2004) studied a bistable mechanism with a curved beam, whereas Klatt et al. (2013) demonstrated negative stiffness behavior and recoverable energy absorption through vertical axial compression in an additively manufactured structure with a curved beam. Correa et al. (2015) optimized the dimensions of NSH, achieving a structure with similar relative density and force threshold as traditional hexagonal honeycomb, but with better energy absorption per unit mass, closely matching the performance of the hexagonal honeycomb. Chen et al. (2021) showed that NSH, comprising curved beams of varying thicknesses, not only improved energy absorption per mass but also enhanced shock absorption and vibration isolation compared to uniform-thickness NSH. Zhang et al. (2021) proposed a lattice and hollow structure for the curved beam, showing better energy dissipation than conventional curved beams of the same volume. Liu et al. (2020) used machine learning methods to achieve enhanced results in curved beam thickness optimization. In addition, research on cylindrical structure (Wang et al., 2020), cubic structure (Ha et al., 2019), and composite negative stiffness structure (Chen et al., 2020) shows various negative stiffness structures and different features depending on the shape and dimensions of NSBs.

A key feature of negative stiffness structures like NSH, distinguishing them from other structures, is their reusability. The studies in Correa et al. (2015), Tan et al. (2019), and

Chen et al. (2020) show the properties of negative stiffness structures, such as force thresholds and energy absorption or dissipation under repeated compression. Chen et al. (2020) shows that the degree of reduction in force threshold for cyclic compression depends on the dimensions of the NSB's thickness. However, there has been limited research on quantifying the performance reduction of negative stiffness structures relative to the NSB dimensions under cyclic compression, which is crucial for predicting the operational end of life (EOL) of these structures.

To address this gap, we propose an integrated design framework that considers both the performance and operational aspects of negative stiffness structures like NSH, including performance degradation. In this study, we targeted the unit cell of NSH for design and manufactured it using PLA/PHA filament through 3D printing. To consider both performance and operational aspects, we conducted quasi-static compression tests and cyclic compression tests to acquire data. Based on this data, we developed a model to estimate the performance and EOL of the NSH unit cell according to its dimensions. Finally, through the Multi-objective Optimization (MOO) design process considering the estimated performance and EOL of the NSH unit cell, we not only confirmed the relationship between the structural performance and operational aspects but also provided insights into the design considering both aspects.

2. DESIGN OF EXPERIMENT

The unit cell of NSH, as illustrated in Figure 1, was employed in this study. The structure of the curved-beam is assumed to be based on Eq. (1). (Qiu et al., 2004) The design variables defined for this structure are the thickness (t) and central height (h) of the curved beam.
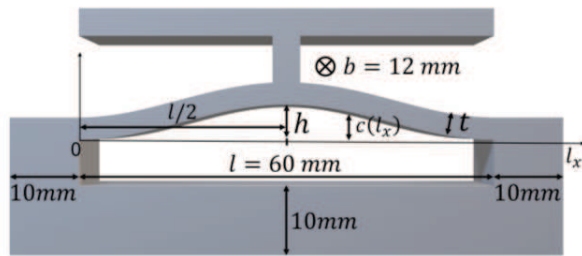

Figure 1. Geometry and dimension of unit cell of NSH

$$c(l_x) = \frac{h}{2}\left[1 - cos\left(2\pi\frac{l_x}{l}\right)\right] \qquad (1)$$

Considering that Zhakatayev et al. (2020) and Tan et al. (2019) have confirmed that the influence of the thickness (t) and height (h) of NSB on the strength, absorbed energy per unit mass, and force threshold of negative stiffness structure, and Qiu et al. (2004) have established a relationship between force-displacement of the curved-beam and geometric parameters as per Eq. (2),

$$F = \frac{3\pi^4 Q^2}{2}d_n\left(d_n - \frac{3}{2} + \sqrt{\frac{1}{4} - \frac{4}{3Q^2}}\right)\left(d_n - \frac{3}{2} - \sqrt{\frac{1}{4} - \frac{4}{3Q^2}}\right) \qquad (2)$$

Klatt et al. (2013) observed that negative stiffness initiates when the numerical value of $Q(= h/t)$ reaches 1.5, when Q exceeds 2.31, the bi-stable characteristics become evident. Therefore, t and h can be considered as important design factors for the negative stiffness structure like Fig 1.

Therefore, we defined the range of t as $1.2[mm] \leq t \leq 3.2[mm]$ and h as $1.2[mm] \leq h \leq 6.4[mm]$. Subsequently, we sampled samples using the design of experiment (DOE) method to train and test the surrogate models and classification models for the characteristics of NSH unit cell, which will be discussed later in section 4 and 5. First, 25 samples were sampled for the training data using the full factorial design (FFD) method. For the test data, 10 samples were sampled through the optimal Latin hypercube design (OLHD) method. The results are illustrated in Figure 2.
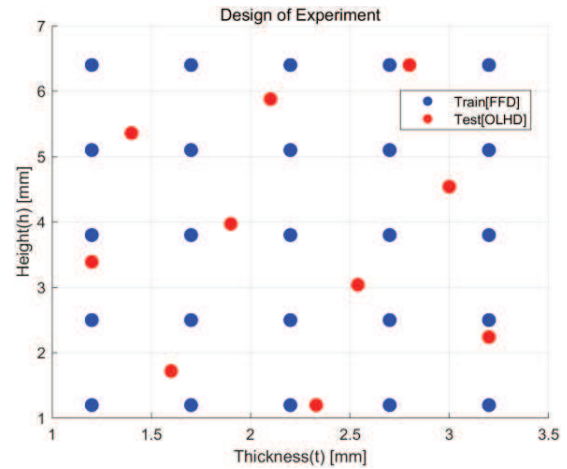

Figure 2. Result of design of experiment

3. FABRICATION AND TEST

We manufactured NSH unit cells with dimensions obtained through the DOE process using a fused filament fabrication (FFF) 3D printer and PLA/PHA filament. Liu et al. (2023) demonstrated that variations in manufacturing features, such as building direction, fill pattern, and wall layers influence printing quality and performance of the NSH cell through the FFF method. Therefore, we considered three different infill angles for 3D printing. We utilized Simplify 3D software for 3D printing, and detailed printing settings can be found in Table 1.

3.1. Material Properties

In this study, Colorfabb's PLA/PHA filament was utilized for fabricating NSH unit cell. Research conducted by Morettni et al. (2022), Letcher & Waytashek et al. (2014), Zouaoui et al. (2021), and Gonabadi et al. (2020) have confirmed that the physical properties of FFF 3D printing can

vary depending on manufacturing parameters such as infill angle or pattern. Therefore, to account for these manufacturing characteristics, five specimens were printed with three different infill angles (0°, 45°, and 90°) to assess the physical properties of the PLA/PHA filament through ASTM D638. An example of specimens is depicted in Figure 3, and the result of ASTM D638 are presented in Table 2.

Table 1. 3D Printing setting.

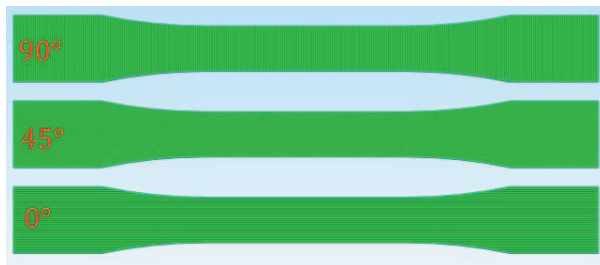| Nozzle Temperature	210 ℃
Bed Temperature	60 ℃
Infill Density	100 %
Infill Pattern	Rectilinear
Infill Angle	[0°, 45°, 90°]
Layer height	0.2 mm
Printing Speed	50 mm/s
Cooling Fan Speed	100 %
Building direction	Flat
Material	PLA/PHA

Figure 3. ASTM D638 specimen with three angles of infill

In Table 2, the average values and standard deviations of the ASTM D638 test results show that the average values of Young's modulus, yield strength, and elongation decreases as the infill angle increases from 0° to 45° and 90°. This is because as the infill angle increases, the force applied to the specimen and the direction of the stacked filament become more closely perpendicular. Therefore, when manufacturing the unit cells of NSH through 3D printing, we set the infill angle to 0° and produced 5 unit cells of NSH per sample. An example is illustrated in Figure 4.

Table 2. Material properties according to infill angles

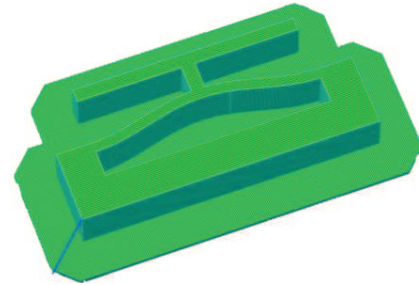| Infill angle	Young's Modulus [GPa]	Yield Strength [MPa]	Elongation [%]	Poisson's Ratio
0°	2.84 (0.059)	52.11 (0.548)	5.84 (1.629)	0.34 (0.005)
45°	2.59 (0.019)	37.86 (0.833)	5.75 (1.561)	-
90°	1.99 (0.062)	16.48 (1.250)	1.65 (0.366)	-

Figure 4. A unit cell for NSH with 0° infill angle

3.2. Compression Test for Data Acquisition

Quasi-static compression tests and cyclic compression tests were conducted to acquire experimental data, considering the performance and operational aspects of the NSH's unit cell. In both tests, compression was applied by inducing a displacement of $2h$ to the unit cell of NSH. The compression test equipment comprised a JSV-1000 stand and a HF-100 force gauge. Additionally, consistent compression test conditions were maintained throughout by securing both ends of the structure using a support structure, as depicted in Figure 5.

Figure 5. Compression test equipment and environment

However, different types of NSH unit cells were utilized in the two types of tests, as shown in Figure 6. The structure depicted in Figure 6 represents a configuration designed for quasi-static compression test. Unlike Figure 1, an additional structure is incorporated at the compression center of the T-shaped support to minimize asymmetric buckling mode in the curved-beam behavior. Conversely, for the cyclic compression test, these additional structures may interfere with the cyclic compression process, hence a configuration similar to Figure. 1 was employed.
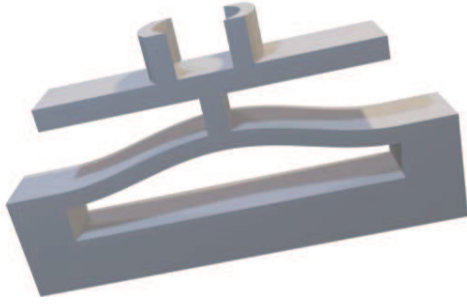
Figure 6. Shape of the NSH unit cell used in quasi-static compression test

3.2.1. Quasi-static Compression Test

To assess the performance aspect of NSH unit cell, a quasi-static compression test was conducted at a speed of 10 mm/min. The obtained force-displacement data were preprocessed using a moving average filter to generate five force-displacement curves for each sample, as illustrated in Figure 7.
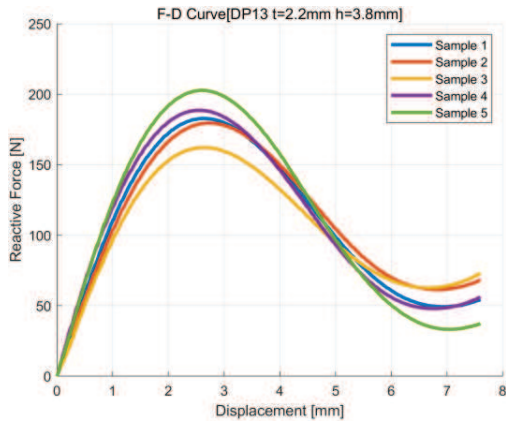

Figure 7. Force-displacement curve for quasi-static compression test

Then, specific energy absorption (SEA) was obtained by dividing Eq. (4) by Eq. (3), with the average SEA value designated as the representative value for the corresponding sample.

$$m = \rho b \left[\left(\int_0^l (c(l_x) + t) dw \right) - \left(\int_0^l c(l_x) \, dw \right) \right] \quad (3)$$

$$EA = \left(\int_0^{2h} f(w) dw \right) \quad (4)$$

These data were also used to examine the occurrence of negative stiffness for five samples of each design point employed in the experiments, as detailed in Section 5. The occurrence of negative stiffness was assessed using Eq. (5), as established by Qiu et al. (2004), and Eq. (6) based on the force-displacement data.

$$w_{mid} = \frac{4}{3} h \quad (5)$$

$$\begin{cases} max_{w<w_{mid}}\big(f(w)\big) - f(w_{mid})) > 0 \rightarrow Negative\ stiffness \\ otherwise \rightarrow Non-Negative\ stiffness \end{cases} \quad (6)$$

This allowed us to classify whether negative stiffness occurred based on w_{mid} in the force-displacement curve.

3.2.2. Cyclic Compression Test

In this experiment, 30 cycles of compression were repeatedly applied at a speed of 60 mm/min. The force-displacement data obtained underwent the same data preprocessing as the quasi-static compression test. The average force-displacement curve for each sample is depicted in Figure 8. Using mean force-displacement data, EA for each cycle was calculated using Eq. (4); mean force-displacement data was also utilized as the health index (HI) for estimating the end of life (EOL), a topic discussed in detail in Section 6.
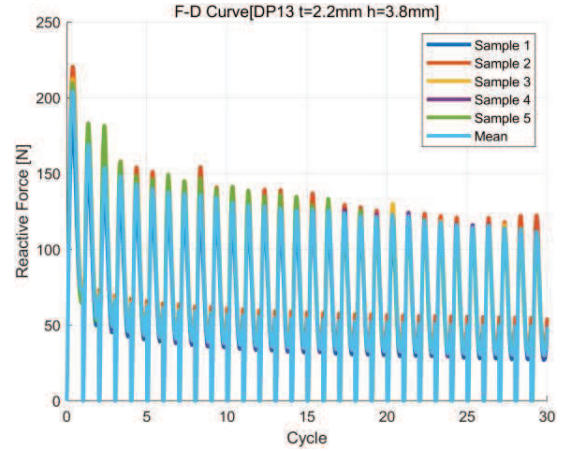

Figure 8. Reactive force for each cycle of the cyclic compression test

4. SURROGATE MODEL

A surrogate model replaces a high-cost test-based or simulation model with a relatively low-cost alternative. By creating a surrogate model for a specific factor of interest, predictions can be made without the need for costly tests or simulations for any given sample. In this study, the Kriging method, implemented in the PIAnO 2024 software, was used to develop a surrogate model for the performance and operational factors of the NSH unit cell. This approach enabled the prediction of the values of these factors for a specific design point.

4.1. Kriging

Kriging is one of the most widely used methods for constructing a surrogate model or metamodel, also known as Gaussian process regression. Based on the references to

Forrester et al. (2008) and Kim et al. (2017), the explanation of Kriging would be as follows: In Kriging, the predicted output of a Kriging model is typically represented as Eq. (7).

$$\hat{y}(\mathbf{x}) = \mathbf{g}(\mathbf{x})^{\mathrm{T}}\boldsymbol{\theta} + \delta(\mathbf{x}) \tag{7}$$

Here, $\mathbf{g}(\mathbf{x})^{\mathrm{T}}\boldsymbol{\theta}$ represents the global function, and $\delta(\mathbf{x})$ represents the local departure. In our study, $\mathbf{x}$ denotes the dimensions of the NSH unit cell, such as t and h, while $\hat{y}$ represents the value we want to predict, such as SEA. We have defined the correlation function for two points $(\mathbf{x}, \mathbf{x}')$ as shown in Eq. (8).

$$\Gamma(\mathbf{x}, \mathbf{x}') = \prod_{i=1}^{ndv} \exp\left(-p_i|x_i - x_i'|^{1.5}\right) \tag{8}$$

where ndv indicates the number of design variables, and p_i represents the parameter of the correlation function. Other types of covariance functions can be found in Rasmussen & Williams (2006) and Xu (2020). Therefore, the correlation matrix is expressed as shown in Eq. (8), and the correlation between the point $\mathbf{x}$ to be predicted and the observed points is expressed as shown in Eq. (9).

$$\Gamma = \begin{pmatrix} \Gamma(\mathbf{x_1}, \mathbf{x_1}) & \cdots & \Gamma(\mathbf{x_1}, \mathbf{x_N}) \\ \vdots & \ddots & \vdots \\ \Gamma(\mathbf{x_N}, \mathbf{x_1}) & \cdots & \Gamma(\mathbf{x_N}, \mathbf{x_N}) \end{pmatrix} \tag{9}$$

$$\boldsymbol{\gamma} = \begin{pmatrix} \Gamma(\mathbf{x_1}, \mathbf{x}) \\ \vdots \\ \Gamma(\mathbf{x_N}, \mathbf{x}) \end{pmatrix} \tag{10}$$

To estimate the parameters of the Kriging model, $\boldsymbol{\theta}$, s^2, and $\mathbf{h}$, we use maximum likelihood estimation (MLE). So, the logarithmic likelihood can be expressed as Eq. (11).

$$\begin{aligned} \ln\left(L(\mathbf{y}|\boldsymbol{\theta}, s^2)\right) \\ = -\frac{N}{2}\ln(2\pi) - \frac{N}{2}\ln(s^2) - \frac{1}{2}\ln(|\boldsymbol{\Gamma}|) \\ - \frac{(\mathbf{y} - \mathbf{G}\boldsymbol{\theta})^{\mathrm{T}}\boldsymbol{\Gamma}^{-1}(\mathbf{y} - \mathbf{G}\boldsymbol{\theta})}{2s^2} \end{aligned} \tag{11}$$

Taking the derivatives of Eq. (11) for $\boldsymbol{\theta}$ and s^2 respectively, and setting them to zero, yields the estimation results via MLE as shown in Eqs. (12) and (13).

$$\hat{\boldsymbol{\theta}} = (\mathbf{G}^{\mathrm{T}}\boldsymbol{\Gamma}^{-1}\mathbf{G})^{-1}(\mathbf{G}^{\mathrm{T}}\boldsymbol{\Gamma}^{-1}\mathbf{y}) \tag{12}$$

$$\hat{s}^2 = \frac{(\mathbf{y} - \mathbf{G}\boldsymbol{\theta})^{\mathrm{T}}\boldsymbol{\Gamma}^{-1}(\mathbf{y} - \mathbf{G}\boldsymbol{\theta})}{2N} \tag{13}$$

The parameter h is determined by substituting Eqs. (12) and (13) into Eq. (11), and the resulting value is maximized by the optimization algorithm (Differential evolution, DE), as expressed in Eq. (14).

$$p = argmax\left[-\frac{N}{2}\ln(\hat{s}^2) - \frac{1}{2}|\boldsymbol{\Gamma}|\right] \tag{14}$$

Given a vector $\hat{\mathbf{y}} = [\mathbf{y}^{\mathrm{T}}, \hat{y}]^{\mathrm{T}}$, which includes the new predicted value $\hat{y}$ at $\mathbf{x}$, the correlation matrix can be written as Eq. (15).

$$\hat{\boldsymbol{\Gamma}} = \begin{pmatrix} \boldsymbol{\Gamma} & \gamma \\ \gamma^{\mathrm{T}} & 1 \end{pmatrix} \tag{15}$$

Based on this, we obtain the logarithmic likelihood, as shown in Eq. (16).

$$\begin{aligned} \ln(L) \\ = -\frac{N}{2}\ln(2\pi) - \frac{N}{2}\ln(\hat{s}^2) - \frac{1}{2}\ln(|\hat{\boldsymbol{\Gamma}}|) \\ - \frac{(\hat{\mathbf{y}} - \mathbf{G}\hat{\boldsymbol{\theta}})^{\mathrm{T}}\hat{\boldsymbol{\Gamma}}^{-1}(\hat{\mathbf{y}} - \mathbf{G}\hat{\boldsymbol{\theta}})}{2\hat{s}^2} \end{aligned} \tag{16}$$

Differentiating Eq. (16) with respect to $\hat{y}$ and setting it to zero, the final output of a Kriging model is expressed as Eq. (17):

$$\hat{y}(\mathbf{x}) = \mathbf{g}(\mathbf{x})^{\mathrm{T}}\hat{\boldsymbol{\theta}} + \boldsymbol{\gamma}(\mathbf{x})^{\mathrm{T}}\boldsymbol{\Gamma}^{-1}(\mathbf{y} - \mathbf{G}\hat{\boldsymbol{\theta}}) \tag{17}$$

4.2. SEA Prediction Model

We formed a surrogate model for SEA to consider the performance aspect of the NSH unit cell. To do this, we first performed a quasi-static compression test on the 25 samples collected by the FFD method, with 5 samples per test point. The average SEA results for each sample were successfully obtained.
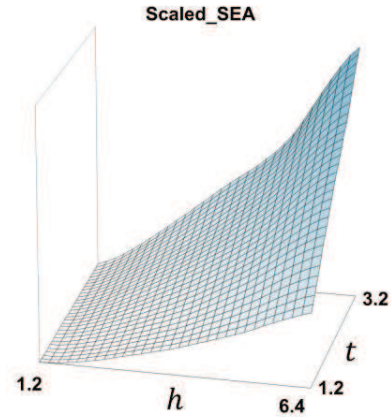

Figure 9. Response surfaced of Scaled SEA_{mean}

Prior to creating the surrogate model using 25 datasets, we set the design variables of the NSH unit cell, t and h, as the inputs for the surrogate model, with SEA_{mean} as the output. Both input and output data were scaled to have values between 0 and 1 using min-max scaling. Finally, we set the global function type to constant, and the results of this surrogate model are depicted in Figure 9. As shown in Figure 9, SEA_{mean} tends to increase as the values of the design variables t and h increase. The root mean square error (RMSE) for this surrogate model was computed using Eq. (18) with 10 test data points, resulting in an RMSE of 0.0276.

$$RMSE = \sqrt{\frac{1}{N}\sum_{i=1}^{N}(y_{pred,i} - y_{true,i})} \qquad (18)$$

4.3. Energy Absorption over Cycles Prediction Model

Similar to Section 4.2, Kriging was utilized to generate surrogate models for predicting EA over the compression cycle using average force-displacement data from about 25 samples collected via FFD method.

Initially, EA for each compression cycle was computed using Eq. (19):

$$EA_{cycle} = \left(\int_{0}^{2h} f_{cycle}(w)dw\right) \qquad (19)$$

Following this, it was assumed that there was no degradation in the NSH unit cell prior to cyclic compression test, and Eq. (20) was used to scale based on 1 cycle of EA as a reference.

$$EA_{sc} = \frac{EA_{cycle}}{EA_{1\,cycle}} \qquad (20)$$

An example of EA_{sc} is shown in Figure 10, where it is crucial to note that for any sample, EA_{sc} is 1 at 1 cycle. EA_{sc} was used as the HI for estimating EOL.
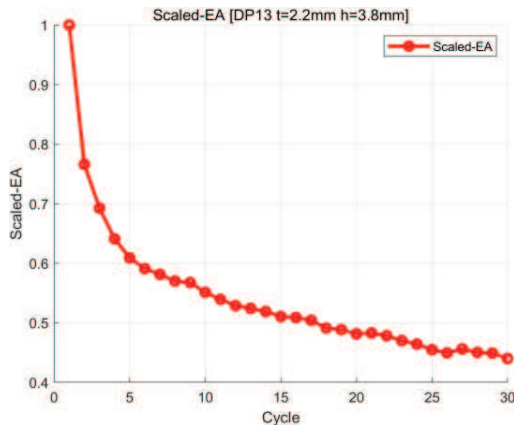

Figure 10. Scaled EA over cycles

The EA_{sc} was further processed by Eq. (21) for samples with a EA_{sc} exceeding 0.9 at 30 cycles:

$$\begin{cases} EA_{sc} = 1, \ for \ cycle = 1 \\ EA_{sc} = EA_{sc-1} - |EA_{sc} - EA_{sc-1}|, otherwise \end{cases} \qquad (21)$$

The input data, consisting of t and h, was used to train the model, aiming to predict EA_{sc} for a specific cycle. Unlike the surrogate model for SEA_{mean}, only min-max scaling was applied to the input data, and a simple quadratic function was utilized as the global function to construct the surrogate model. The corresponding response surface for this is shown in Figure 11.
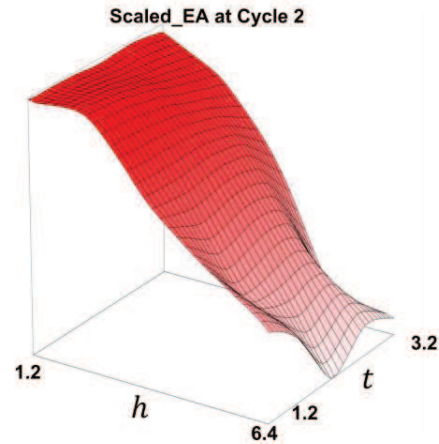

Figure 11. Response surfaced of EA_{sc} at cycle 2

The surrogate model predicts EA_{sc} for each cycle, which is then utilized to estimate the EOL for NSH unit cells. This will be discussed in detail in Section 6.

5. CLASSIFICATION MODEL

A classification model was developed based on the findings discussed in Section 3.2.1, where the design of NSH unit cells exhibits negative stiffness depending on certain design variables. Previous studies by Shahan et al. (2012), Morris et al. (2018), and Matthews et al. (2016) demonstrated that a set-based approach using the Bayesian network classifier method can be used to explore the boundaries of the design space and identify designs that meet specific performance criteria. Based on this, we utilized the Bayesian classifier as a classification model to determine the presence of negative stiffness. We formed the classification model using the results from quasi-static compression tests on 25 samples. Furthermore, this classification model was used as a constraint in the MOO design process, which will be discussed in detail in Section 7.

5.1. Bayes classifier

The results from all five test points in the quasi-static compression test were incorporated into the Bayesian classifier model. Specifically, the prior probability, as defined by Eq. (22) from Shahan et al. (2012), was established based on the frequency of occurrence of negative stiffness.

$$\begin{cases} P(c_{NS}) = \dfrac{N_{NS} + 1}{N + 2} \\ P(c_{NNS}) = \dfrac{N_{NNS} + 1}{N + 2} \end{cases} \qquad (22)$$

For the likelihood, multivariate kernel density estimation was employed as described by Scott (2015) and can be expressed using Eq. (23):

$$\begin{cases} P(\mathbf{x}|c_{NS}) = \dfrac{1}{N_{NS}\beta_{1,NS}\cdots\beta_{N_d,NS}}\sum_{i=1}^{N_{NS}}\left\{\prod_{j=1}^{N_d}K\left(\dfrac{x_j - x_{ij}}{\beta_j}\right)\right\} \\ P(\mathbf{x}|c_{Non-NS}) = \dfrac{1}{N_{NNS}\beta_{1,NNS}\cdots\beta_{N_d,NNS}}\sum_{i=1}^{N_{NNS}}\left\{\prod_{j=1}^{N_d}K\left(\dfrac{x_j - x_{ij}}{\beta_j}\right)\right\} \end{cases} \quad (23)$$

The Gaussian kernel K is used, and the bandwidth β values are calculated using Eq. (24):

$$\begin{cases} \beta_{j,NS} = s_j\left\{\dfrac{4}{(N_d + 2)N_{NS}}\right\}^{1/(N_d+4)} \\ \beta_{j,NNS} = s_j\left\{\dfrac{4}{(N_d + 2)N_{NNS}}\right\}^{1/(N_d+4)} \end{cases} \quad (24)$$

The posterior probabilities for the two classes are given by Eq. (25).

$$\begin{cases} P(c_{NS}|\mathbf{x}) = P(c_{NS})P(\mathbf{x}|c_{NS}) \\ P(c_{NNS}|\mathbf{x}) = P(c_{NNS})P(\mathbf{x}|c_{NNS}) \end{cases} \quad (25)$$

$$\lambda_1 P(c_{NS})P(\mathbf{x}|c_{NS}) - \lambda_2 P(c_{NNS})P(\mathbf{x}|c_{NNS}) > 0 \quad (26)$$

Then, the decision rule for class for classifying a sample regarding the occurrence of negative stiffness is defined by Eq. (26) below. According to the study by Shahan et al. (2012), it has been confirmed that the loss factor λ_1 and λ_2 can shift the decision boundary of the classifier. Therefore, setting $\lambda_1 = 0.66$, $\lambda_2 = 0.34$ accounts for cases where negative and non-negative stiffness may occur simultaneously in the samples. This setting allows the classification of such samples into the class indicating the occurrence of negative stiffness. With $\lambda_1 = 0.66$ and $\lambda_2 = 0.34$, the difference between the two posterior probabilities is illustrated in Figure 12.
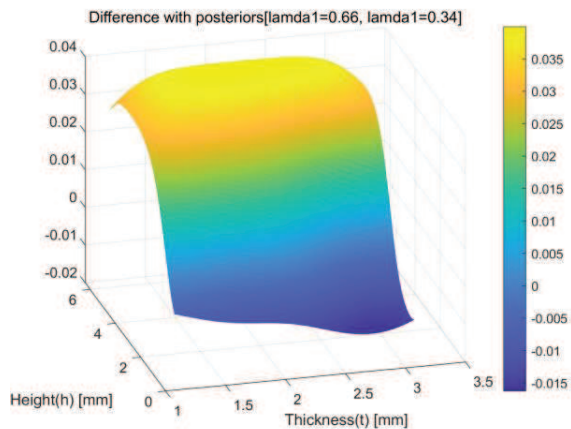

Figure 12. Difference between the two posterior probabilities

6. PREDICTING EOL OF NSH UNIT CELL

In order to consider the operational aspects of the NSH unit cell, prognostics methods were utilized to estimate the EOL. According to Kim et al. (2017), prognostics methods can be categorized into physics-based and data-driven approaches. Kim et al. (2017) also introduced nonlinear least square (NLS), Bayesian method (BM), and particle filter (PF) within physics-based prognostics. In this study, the NLS method

demonstrated by Kim et al. (2017) was used to estimate the EOL by considering degradation, as shown in Figure 10, through EA_{sc}, which serves as the HI of the NSH unit cell.

First, to estimate the EOL via NLS, the degradation equation was defined as Eq. (27):

$$\varphi = exp\left(-|\xi_1| \cdot (cycle - 1)^{\xi_2}\right) \quad (27)$$

The parameters ξ_1 and ξ_2 were estimated using the 'lsqnonlin' function in MATLAB R2023b, employing the Levenberg-Marquardt method. To consider the uncertainty of the estimated model parameters in NLS, the 95% confidence intervals for the model parameters were obtained from 1.0E7 random sampling from the multivariate t-distribution using Eqs. (28) and (29), with degrees of freedom $N - N_p + 1$. Here, Eq, (28) represents the variance of noise in measured data, and Eq. (29) represents the variance of estimated model parameters.

$$s_n^2 = \frac{\{\mathbf{y} - \boldsymbol{\varphi}\}^T\{\mathbf{y} - \boldsymbol{\varphi}\}}{N - N_p} \quad (28)$$

$$\mathbf{M}_\xi = s_n^2[\boldsymbol{\Psi}^T\boldsymbol{\Psi}]^{-1} \quad (29)$$

The challenge in EOL estimation lies in determining amount of EA_{sc} data needed to estimate the EOL using the surrogate model from Section 4.3, and how to estimate parameters ξ_1 and ξ_2 using NLS. To address this, a model was developed to predict EA_{sc} for design variables t and h across 2 to 15 cycles using the Kriging model from Section 4.3. For the 10 test data, the EA_{sc} data estimated by the surrogate model from 3 to 15 cycles was progressively added, calculating the median of the confidence interval of NLS and the mean RMSE of the actual experimental data. The results of mean RMSE are depicted in Figure 13.
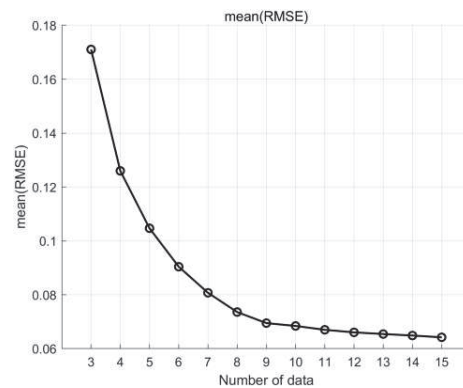

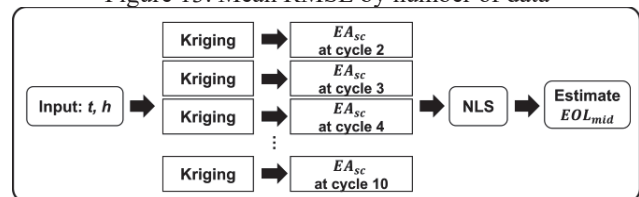Figure 13. Mean RMSE by number of data

Figure 14. EOL Estimation Process

It was observed that utilizing more than 10 cycles of data predicted from surrogate model (i.e., beyond 1-10 cycles) did not significantly affect the estimation error in degradation estimation via NLS. Consequently, EA_{sc} values were estimated for 2-10 cycles through a surrogate model as shown in Figure 11, considering that at 1 cycle, the EA_{sc} value is consistently 1 across all samples. This process is illustrated in Figure 14. Therefore, this process was utilized to estimate the EOL of the NSH unit cell, and the median of the EOL confidence interval (EOL_{mid}) was used in the MOO design process, which will be discussed in detail in Session 7.

7. MULTI-OBJECTIVE OPTIMIZATION DESIGN

A MOO design was implemented to address both the performance and operational aspects of the NSH unit cell. SEA_{mean} was considered for the performance aspect, while the estimated EOL_{mid} served as the objective function for the operational aspect. Constraints included the strain of the curved beam, the threshold for HI, and the presence or absence of negative stiffness. The problem was formulated accordingly, and the results of the MOO design were analyzed using the NSGA-2 optimization algorithm (Deb et al., 2002), implemented in the PIAnO 2024 software. The overall flowchart is depicted in Figure 15.
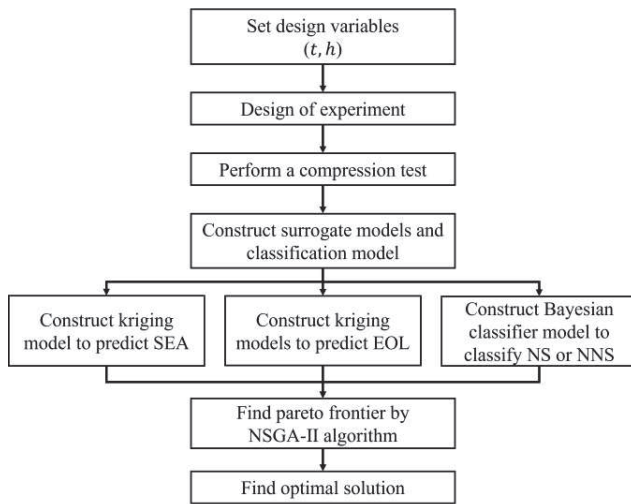

Figure 15. Flowchart of multi-objective optimization design

7.1. Problem Formulation

For the MOO design, the problem formulation is defined as Eq. (30). Initially, the surrogate model for SEA_{mean}, as discussed in Section 4.2, was employed to address the performance aspect of the NSH unit cell. Maximizing the SEA_{mean} implied enhancing the capacity of the unit's curved beam to absorb energy relative to its mass. Subsequently, the EOL_{mid} estimated through the approach outlined in Section 6, was considered for the operational aspect. To ensure comparability in scale between the scaled SEA_{mean} by min-max scaling and the estimated EOL_{mid}, we utilized the EA_{sc}

obtained from cyclic compression tests from 1 to 30 cycles on the 25 samples extracted using the FFD method to estimate EOL_{mid}. Based on this estimation, we performed min-max scaling on the estimated EOL_{mid}. At this point, it was assumed that the EOL_{mid} from 25 samples provides sufficient information about EOL_{mid} for the entire design space.

The first constraint was defined using the maximum strain, determined from the mean elongation when the infill angle is 0°. The second constraint was defined as the occurrence of negative stiffness, where $\lambda_1 = 0.66$ and $\lambda_2 = 0.34$. The threshold for EA_{sc} as HI was assumed to be 0.7, indicating that the structure has degraded to 30% of its original performance.

$$
\begin{aligned}
&Find \quad\quad t, h \\
&maximize \quad f(\mathbf{x}) \\
&\quad\quad\quad\quad = SEA_{sc,mean}(t_{sc}, h_{sc}) \\
&\quad\quad\quad\quad + EOL_{sc,mid}(t_{sc}, h_{sc}) \\
&subject\ to \quad 2\pi^2 \frac{th}{l^2} < 0.0584 \\
\\
&\quad\quad 0.66 P(c_{NS})P(t,h|c_{NS}) \\
&\quad\quad - 0.34 P(c_{NNS})P(t,h|c_{NNS}) > 0 \\
\\
&\quad\quad Threshold = 0.7 \\
\\
&\quad\quad 1.2\ mm \le t \le 3.2\ mm \\
\\
&\quad\quad 1.2\ mm \le h \le 6.4\ mm
\end{aligned}
\tag{30}
$$

7.2. Result of Multi-Objective Optimization Design

In the MOO design process, we considered an initial design point for the NSH unit cell with $t = 2.2\ mm$ and $h = 3.8\ mm$. NSGA-2 was employed as the optimization algorithm in the PIAnO 2024 software, with settings summarized in Table 3.

Table 3. The settings for NSGA-2

Population Size	100
Crossover Rate	0.9
Mutation Rate	0.5
Maximum Number of Generations	250

The results are displayed in Figure 16, where the lower constraints pertain to the condition for the occurrence of negative stiffness, while the upper constraints relate to the maximum strain. When plotting the Pareto frontier for the objective function, it appears similar to Figure 17.
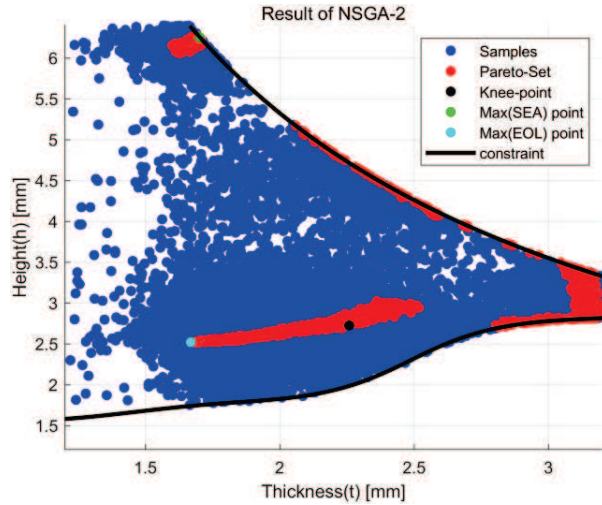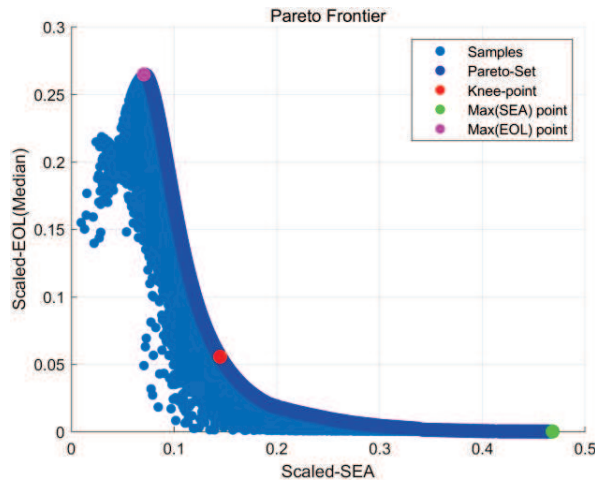
Figure 16. Optimum results using NSGA-2

Figure 17. Results of Pareto frontier

Figure 17 illustrates that, despite aiming to maximize the objective functions, EOL and SEA exhibit an inverse relationship within the Pareto optimal set. As EOL increases, SEA decreases, and vice versa. Therefore, to identify the knee point, a horizontal line was extended from the point with the maximum SEA_{mean}, and a vertical line from the point with the maximum EOL_{mid}. The knee point was determined as the intersection of these lines, selected as the closest point from the Pareto optimal set. The dimensional information for the points with the maximum SEA_{mean}, maximum EOL_{mid}, and the knee point is provided in Table 4.

Table 4. Dimensions for three points

	Max (SEA_{mean})	Max (EOL_{mid})	Knee Point
t [mm]	1.702	1.669	2.258
h [mm]	6.255	2.52	2.725

After manufacturing, quasi-static compression tests and cyclic compression tests were conducted for these three points, as discussed in Section 3. All three points satisfied maximum strain constraint as defined in Eq. (29) and exhibited negative stiffness in five samples per point during the test. The results for SEA_{mean} and EOL_{mid} were summarized in Tables 5 and 6.

Table 5. SEA_{mean} results of 3 points

	Initial point	Max (SEA_{mean})	Max (EOL_{mid})	Knee point
True [mJ/g]	425.96	641.06	116.05	207.34
Predict [mJ/g]	-	760.93	128.27	246.42

Table 6. Estimated EOL_{mid} results of 3 points

	Initial point	Max (SEA_{mean})	Max (EOL_{mid})	Knee point
Estimated EOL_{mid} [95% C.I] by proposed method (Cycle)	-	1.49 [1.47 ,1.52]	102.08 [50.21, 266.95]	22.56 [14.78, 39.04]
Estimated EOL_{mid} from 30 cycles of true test data (Cycle)			127.91	31.44
True EOL (Cycle)	2.90	1.48	-	-

According to Table 5, the SEA_{mean} value at the point where it reaches its maximum is approximately 50.5% higher than the initial design point, as predicted by the surrogate model.

Table 6 displays the estimated EOL_{mid} results for the three points. The median result estimated by the proposed method was compared with actual compression test data collected over 30 cycles. However, it is important to note that since cyclic compression test data are available only up to 30 cycles, the EOL beyond this point cannot be accurately determined. Therefore, for the three design points, considering the average RMSE of 0.0073 between the NLS results using actual data from 1 to 30 cycles and the actual data, it is assumed that the extrapolated median results using the NLS method do not significantly differ from the actual EOL. The results presented in Table 6 demonstrate that the EOL_{mid} obtained with the actual data falls within the 95% confidence interval of the EOL estimated by the proposed method.

When comparing the maximum EOL_{mid} point with the initial point, Table 6 shows an increase of approximately 99.17 cycles in EOL_{mid}, based on the estimated EOL_{mid} in

the operational aspect. However, there is a notable decrease of about 72.75% in SEA_{mean}, representing the performance aspect. This trend is also observed at the knee point, where the operational aspect shows an EOL_{mid} increase of approximately 19.66 cycles, but a performance decrease of around 51.32% in SEA_{mean}. These observations highlight the trade-off between SEA_{mean} (performance) and EOL_{mid} (operational aspect, including degradation) in NSH unit cells. The initial design point has a high SEA_{mean} value but a very low EOL_{mid} value in terms of service life, presenting a risk of breakage in case of repeated use. The results of the MOO show that the expected EOL_{mid} result for the SEA value at the initial design point and the corresponding value is 4.72 cycles at $t = 3.147$ mm $h = 2.926$ mm, which is an improvement in life and performance compared to the initial design point.

Moreover, analyzing the data from Tables 5 and 6, it can be inferred that if the target life is set to 20 cycles, the knee point emerges as the most reasonable design, considering the estimated EOL_{mid}. Conversely, if reusability is not a priority, the point with the maximum SEA_{mean} value appears to be the optimal design choice. Consequently, this suggests that the most reasonable design can be determined from the Pareto optimum set, depending on the target life set by the designer.

8. CONCLUSION

In this study, a novel design framework for NSH unit cells was proposed, focusing on energy absorption and reusability. SEA_{mean} was considered as a performance metric, while EOL_{mid} estimation relied on operational degradation from cyclic compression. Using the repeated compression test data of 3D-printed NSH unit cell, a trade-off relationship between SEA_{mean} and EOL_{mid} was identified through Pareto frontier analysis employing the NSGA-2 optimization algorithm. From the MOO results, it is evident that establishing a criterion for the target life enables the identification of a viable design point for that lifespan. This approach not only facilitates the lifespan-oriented design of NSH unit cells but also highlights the potential for its application in the design of multi-layer NSHs or similar negative stiffness structures. In the application of these structures, the lifespan of the structure is factored into the design process so that the time to repair or replace the structure can be considered and reflected in the design phase. This framework can be expected to facilitate decision-making based on information about the predicted health of the structure at the design stage and provide possibilities for prognostics and health management (PHM) for design.

Finally, future work aims to develop a PHM framework for robust design that can account for uncertainties or noise that may occur during the manufacturing process and in the testing or operational environment, as efforts continue to predict the health more precisely and EOL of these structures.

ACKNOWLEDGEMENT

NOMENCLATURE

t	thickness of curved beam
h	central height of curved beam
t_{sc}	scaled thickness of curved beam
h_{sc}	scaled central height of curved beam
Q	t/h
c	height of curved beam for length
l	length of curved beam (= 60 mm)
l_x	horizontal length of curved beam (= 0 ~ 60 mm)
b	width of curved beam (= 12 mm)
ρ	density of PLA/PHA filament (= 1.24 g/cm^3)
F	normalized force
f	reactive force
w	displacement
d_n	normalized displacement (= w/h)
m	mass of curved beam
ξ	parameter of degradation equation
$\boldsymbol{\theta}$	global function's coefficients
p	parameter of correlation function
L	likelihood
m	mass
σ^2	variance
y	observed data
y_{pred}	predicted value
y_{true}	true value
$\hat{y}$	output of Kriging
EA_{SC}	Scaled EA from original data
N	number of observations
N_{NS}	number of negative stiffness occurrences
N_{NNS}	number of non-negative stiffness occurrences
N_d	number of dimensions
N_p	number of parameters
c_{NS}	class for occurrence of negative stiffness
c_{NNS}	class for occurrence of non-negative stiffness
s	standard deviation
$\boldsymbol{\Psi}$	Jacobian matrix
n_p	number of parameters
β	bandwidth
$\mathbf{g}$	bases of global function
$\mathbf{G}$	Matrix of bases of global function
$\mathbf{M}_\xi$	variance of parameters for degradation equation
$\boldsymbol{\Gamma}$	correlation matrix
$\boldsymbol{\gamma}$	correlation vector
$\mathbf{x}$	vector of design variables t and h

REFERENCES

Chen, S., Wang, B., Zhu, S., Tan, X., Hu, J., Lian, X., Wang, L., & Wu, L. (2020). A novel composite negative stiffness structure for recoverable trapping energy. *Composites Part A: Applied science and*

manufacturing, *129*, 105697. doi: 10.1016/j.compositesa.2019.105697

Correa, D.M., Klatt, T., Cortes, S., Haberman, M., Kovar, D. & Seepersad, C. (2015), Negative stiffness honeycombs for recoverable shock isolation, Rapid Prototyping Journal, Vol. 21 No. 2, pp. 193-200. Doi: 10.1108/RPJ-12-2014-0182

Correa, D.M., Seepersad, C.C. & Haberman, M.R. (2015), Mechanical design of negative stiffness honeycomb materials. *Integr Mater Manuf Innov* **4**, 165–175. doi: 10.1186/s40192-015-0038-8

Deb, K., Agrawal, S., Pratap, A., & Meyarivan, T. (2000). A fast elitist non-dominated sorting genetic algorithm for multi-objective optimization: NSGA-II. In *Parallel Problem Solving from Nature PPSN VI: 6th International Conference,* September 18–20, Paris, France. doi:10.1007/3-540-45356-3_83

Debeau, D. A., Seepersad, C. C., & Haberman, M. R. (2018). Impact behavior of negative stiffness honeycomb materials. *Journal of Materials Research*, *33*(3), 290–299. doi:10.1557/jmr.2018.7

Gonabadi, H., Yadav, A. & Bull, S.J. (2020). The effect of processing parameters on the mechanical characteristics of PLA produced by a 3D FFF printer. *Int J Adv Manuf Technol* **111**, 695–709. doi:10.1007/s00170-020-06138-4

Ha, C. S., Lakes, R. S., & Plesha, M. E. (2019). Cubic negative stiffness lattice structure for energy absorption: Numerical and experimental studies. *International Journal of Solids and Structures*, *178*, 127-135. doi: 10.1016/j.ijsolstr.2019.06.024.

Klatt, T. Michael, H. Seepersad, C.C. (2013), Selective Laser Sintering of Negative Stiffness Mesostructures for Recoverable, Nearly-Ideal Shock Isolation, *2013 cInternational SFF Symposium*, August 12-14, Austin, doi:10.26153/tsw/15653

Kim, N. H., An, D., & Choi, J. H. (2017). Prognostics and health management of engineering systems. Switzerland: Springer International Publishing.

Letcher, T, & Waytashek, M. (2014) "Material Property Testing of 3D-Printed Specimen in PLA on an Entry-Level 3D Printer." *Proceedings of the ASME 2014 International Mechanical Engineering Congress and Exposition*. November 14–20, Montreal, Quebec, Canada. doi:10.1115/IMECE2014-39379

Liu, F., Jiang, X., Wang, X., & Wang, L. (2020). Machine learning-based design and optimization of curved beams for multistable structures and metamaterials. *Extreme Mechanics Letters*, *41*, 101002. doi: 10.1016/j.eml.2020.101002

Liu, Y., Jiang, W., Hu, W., Ren, L., Deng, E., Wang, Y., Song, C. & Feng, Q. (2023). Compressive strength and energy absorption characteristics of the negative stiffness honeycomb cell structure. *Materials Today Communications*, *35*, 105498. doi: 10.1016/j.mtcomm.2023.105498

Matthews, J., Klatt, T., Morris, C., Seepersad, C. C., Haberman, M. & Shahan, D. (2016). Hierarchical Design of Negative Stiffness Metamaterials Using a Bayesian Network Classifier. ASME. *J. Mech. Des*. 138(4): 041404. doi:10.1115/1.4032774

Morris, C., Bekker, L., Haberman, M. R. & Seepersad, C. C. (2018). Design Exploration of Reliably Manufacturable Materials and Structures With Applications to Negative Stiffness Metamaterials and Microstereolithography. ASME. *J. Mech. Des*. 140(11): 111415. doi:10.1115/1.4041251

Rasmussen, C. E. & Williams, C. K. (2006). Gaussian processes for machine learning. Cambridge, MA: MIT press.

Shahan, D. W. & Seepersad, C. C. (2012). Bayesian Network Classifiers for Set-Based Collaborative Design. ASME. *J. Mech. Des*. 134(7): 071001. doi:10.1115/1.4006323

Shan, S., Kang, S.H., Raney, J.R., Wang, P., Fang, L., Candido, F., Lewis, J.A. & Bertoldi, K. (2015), Multistable Architected Materials for Trapping Elastic Strain Energy. Adv. Mater., 27: 4296-4301. doi:10.1002/adma.201501708

Scott, D. W. (2015). Multivariate density estimation: theory, practice, and visualization. John Wiley & Sons.

Tan, X., Chen, S., Zhu, S., Wang, B., Xu, P., Yao, K., & Sun, Y. (2019). Reusable metamaterial via inelastic instability for energy absorption. *International Journal of Mechanical Sciences*, *155*, 509-517. doi: 10.1016/j.ijmecsci.2019.02.011

Wang, B., Tan, X., Zhu, S., Chen, S., Yao, K., Xu, P., Wang, L., Wu, H. & Sun, Y. (2019). Cushion performance of cylindrical negative stiffness structures: Analysis and optimization. *Composite Structures*, *227*, 111276. doi: 10.1016/j.compstruct.2019.111276

Xu, H. (2020). Constructing Oscillating Function-Based Covariance Matrix to Allow Negative Correlations in Gaussian Random Field Models for Uncertainty Quantification. ASME. J. Mech. Des. 142(7): 074501. doi:10.1115/1.4046067

Zhakatayev, A., Kappassov, Z., & Varol, H. A. (2020). Analytical modeling and design of negative stiffness honeycombs. *Smart Materials and Structures*, *29*(4), 045024. doi:10.1088/1361-665X/ab773a

Zouaoui, M., Gardan, J., Lafon, P., Makke, A., Labergere, C., & Recho, N. (2021). A finite element method to predict the mechanical behavior of a pre-structured material manufactured by fused filament fabrication in 3D printing. *Applied Sciences*, *11*(11), 5075. doi:10.3390/app11115075

BIOGRAPHIES

Hyung-Do Kim is currently an integrated MS and Ph.D student at Pusan National University, Busan, South Korea. He received his B.S. degree in department of

mechanical engineering from Kyonggi University, Suwon, South Korea, in 2022. His research interests include data driven design and design for manufacturing.

Taemin Noh is currently a MS student at Pusan National University, Busan, South Korea. He received his B.S. degree in department of mechanical engineering from Pusan National University, Busan, South Korea, in 2022. His research interests include data driven design and design for manufacturing.

Young-Jin Kang received the Ph.D. degree in mechanical engineering from Pusan National University, Busan, South Korea. He has been working as a postdoctoral researcher in Research Institute of Mechanical Technology, Pusan National University, Korea. His research area is uncertainty quantification, design under uncertainties, data driven design, and fault detection and diagnosis.

Nam-Ho Kim received his Ph.D. degree in mechanical engineering from University of Iowa, United States. He has been working as a professor in the Department of Mechanical engineering at University of Florida, Gainesville, United States. His research areas include design under uncertainty, prognostics and health management, uncertainty quantification, and nonlinear structural mechanics.

Yoojeong Noh received the Ph.D. degree in mechanical engineering from University of Iowa, United States. She has been working as an associate professor in the school of mechanical engineering in Pusan National University, Busan, South Korea. Her research interests include computational mechanics, design under uncertainties, data driven design, and fault detection and diagnosis.